

1    **Developing a holistic understanding of monsoon formation with idealized**  
2                                    **model simulations and theories**

3                                    Jane E. Smyth\* and Yi Ming<sup>†</sup>

4                    *Program in Atmospheric and Oceanic Sciences, Princeton University, Princeton, NJ*

5    \**Corresponding author address:* Jane E. Smyth, Program in Atmospheric and Oceanic Sciences,  
6    300 Forrestal Rd., Princeton, NJ 08540.

7    E-mail: jsmyth@princeton.edu

8    <sup>†</sup>Geophysical Fluid Dynamics Laboratory/NOAA, 201 Forrestal Road, Princeton, NJ 08540.

## ABSTRACT

9 Monsoons emerge over a range of land surface conditions and exhibit vary-  
10 ing physical characteristics over the seasonal cycle, from onset to withdrawal.  
11 Systematically varying the moisture and albedo parameters over land in an  
12 idealized modeling framework allows one to analyze the physics underlying  
13 the successive stages of monsoon development. To this end we implement  
14 an isolated South American continent with reduced heat capacity, but no to-  
15 pography in an idealized moist general circulation model. Irrespective of the  
16 local moisture availability, the seasonal cycles of precipitation and circulation  
17 over the South American monsoon sector are distinctly monsoonal with the  
18 default surface albedo. The dry land case (zero evaporation) is characteristic  
19 of a shallow overturning circulation with vigorous lower-tropospheric ascent,  
20 transporting water vapor from the ocean. By contrast, the monsoon dynamics  
21 with bucket hydrology or unlimited land moisture features deep moist convec-  
22 tion that penetrates the upper troposphere. A series of land albedo perturba-  
23 tion experiments indicates that the monsoon strengthens with the net column  
24 energy flux and the near-surface moist static energy with all land moisture  
25 conditions. The analysis supports that when the land-ocean thermal contrast  
26 is strong enough, inertial instability alone is sufficient for producing a shal-  
27 low but vigorous circulation and converging a large amount of moisture from  
28 the ocean even in the absence of land moisture. Once the land is sufficiently  
29 moist, convective instability takes hold and the shallow circulation deepens.  
30 These results have implications for monsoon onset and intensification, and  
31 may elucidate the seasonal variations in how surface warming impacts tropi-  
32 cal precipitation over land.

## 33 1. Introduction

34 Monsoon circulations play a key role in Earth’s climate, including the atmospheric energy, mois-  
35 ture, and momentum budgets. They are the defining feature of the seasonal cycle over tropical land,  
36 producing rain in local summer and dry conditions in winter. Consequently, monsoon variability  
37 carries great social and economic significance, with agriculture, energy systems, and ecosystem  
38 health all depending on monsoon regularity. Over 70% of the world’s population is directly im-  
39 pacted by monsoon variability, which can cause droughts, floods, food insecurity, worsened wild-  
40 fires, energy shortages, and broad financial impacts (An et al. 2015).

41 The theoretical and societal importance of monsoons has motivated sustained research efforts  
42 to identify the key mechanisms underlying their development and regulation. The traditional con-  
43 ception of monsoons as land-sea breezes has given way to the modern perspective of monsoons  
44 as an integral component of the global atmospheric circulation and climate. Studies applying the  
45 axisymmetric theory for the Hadley cells to idealized monsoons have driven this shift in thinking  
46 (Privé and Plumb 2007a,b; Bordoni and Schneider 2008). Based on theory for angular momentum  
47 conserving circulations, Privé and Plumb (2007a,b) link the meridional extent of the monsoonal  
48 overturning cell to the near-surface maximum of subcloud moist static energy (MSE), and find  
49 that this is a good indicator of the monsoon extent even when zonal symmetry is broken. They  
50 utilize the MITGCM with Newtonian cooling and prescribed SSTs. Bordoni and Schneider (2008)  
51 describe a rapid summertime transition to off-equatorial tropical convergence in an idealized moist  
52 aquaplanet model with a two-stream gray radiation scheme. This indicates that land-sea thermal  
53 contrast is not fundamental to monsoon emergence. They characterize monsoons as a regime tran-  
54 sition of the Hadley circulation: during the monsoon season, the cross-equatorial winter Hadley  
55 cell is in an angular momentum-conserving regime, subject to little influence by extratropical ed-

56 dies. The alignment of streamlines with angular momentum contours over the Indian monsoon  
57 sector suggests the potential utility of this theory for off-equatorial monsoons (Walker and Bor-  
58 doni 2016).

59 There are three primary theoretical conceptions of monsoons in the literature: one based on  
60 convective quasi-equilibrium (CQE), another founded on the moist static energy budget, and one  
61 that frames the monsoon as an extension of the zonal-mean ITCZ (Hill 2019). In the CQE view, the  
62 monsoonal overturning cell extends to the latitude of highest near-surface MSE, with the maximum  
63 rainfall located just equatorward thereof (e.g. Privé and Plumb 2007a,b; Nie et al. 2010; Hurley  
64 and Boos 2013). CQE posits that convection couples near-surface and upper tropospheric MSE,  
65 linking high boundary layer MSE to high upper-tropospheric potential temperatures (Emanuel  
66 and Bretherton 1994). Within this framework, the impact of a perturbation on the monsoon can be  
67 understood via its effect on the near-surface thermodynamics. While useful, the CQE paradigm  
68 provides little prognostic power in the absence of a complete theory for what controls the near-  
69 surface MSE distribution itself.

70 Alternatively, some studies use the column-integrated MSE budget as a basis for characterizing  
71 tropical rainfall, including monsoon circulations (e.g. Neelin and Held 1987; Chou and Neelin  
72 2004; Back and Bretherton 2006; Neelin 2007; Hill et al. 2017). The MSE budget, presented in  
73 detail in Section 3b, states that the net column forcing from radiative and turbulent heat fluxes must  
74 balance the atmospheric MSE flux divergence and the time tendency of column-integrated internal  
75 energy. While MSE budget analysis is a diagnostic approach, it has been applied in various fruitful  
76 ways, such as: to evaluate the limits on the poleward extent of monsoons (e.g. Chou and Neelin  
77 2001); to identify key mechanisms of tropical precipitation change, such as the “upped-ante” and  
78 “rich-get-richer” responses (Chou and Neelin 2004); and to assess a circulation’s susceptibility to  
79 these responses under climate change (Hill et al. 2017; Smyth and Ming 2020).

80 Unlike the local control of precipitation in the CQE and MSE budget theories, the ITCZ frame-  
81 work takes a unified view of land and ocean precipitation as guided by zonal mean energetics  
82 (Chao and Chen 2001). This perspective is consistent with a global monsoon mode that encom-  
83 passes the solstitial migrations of the convergence zone across the regional subsystems (Geen  
84 et al. 2020). The ITCZ is the tropical rainfall maximum whose location is determined by the  
85 cross-equatorial extent of the Hadley circulation, which in turn is guided by the energy flux equa-  
86 tor, the zero-crossing of the meridional atmospheric heat transport (Kang et al. 2008). The ITCZ  
87 shifts towards the hemisphere with higher net energy input to the atmosphere, allowing anomalous  
88 energy transport to the opposite hemisphere by the upper branch of the cross-equatorial Hadley  
89 cell (e.g. Bischoff and Schneider 2014). On paleoclimate timescales, the Indian monsoon com-  
90 plies with ITCZ constraints, migrating towards asymmetric hemispheric warming (Schneider et al.  
91 2014), and on an interannual basis, a strong Indian monsoon is associated with northward migra-  
92 tions of the meridional overturning circulation (Walker et al. 2015). As in CQE theory, the view  
93 of monsoons as a regional extension of the thermally-direct Hadley circulation highlights the role  
94 of near-surface MSE gradients, rather than temperature gradients, in modulating the monsoon  
95 strength and position (Walker et al. 2015). It is also worth noting that the ITCZ over land and  
96 ocean may shift in opposite directions in certain situations, hinting at potential limitations of the  
97 ITCZ framework (Hill 2019; Smyth et al. 2018).

98 It is not straightforward to assess the role of land surface properties within any of the afore-  
99 mentioned monsoon theories. Vegetation impacts both albedo and moisture fluxes, driving feed-  
100 backs between rainfall changes and ecological transitions (Charney 1975). Soil moisture has im-  
101 plications for the partitioning of surface turbulent fluxes, and therefore the surface temperature,  
102 precipitation, and regional circulation (e.g. Seneviratne et al. 2010). In regions with strong land-  
103 atmosphere coupling, including India, West Africa, and parts of tropical South America (Koster

et al. 2004), soil moisture strongly impacts the evaporative fraction and daily maximum surface temperature (Schwingshackl et al. 2018). Zhou and Xie (2018) utilize an idealized model with gray radiation to evaluate the role of geometry, albedo, soil moisture, and ocean heat fluxes on monsoon properties. They find that with the exception of soil moisture, all these factors can be understood via their effects on the surface equivalent potential temperature ( $\theta_e$ , essentially MSE) distribution, underscoring the importance of CQE dynamics. In their experiments, soil moisture changes elicit more complex circulation responses that are not always consistent with the migration of the maximum near-surface MSE, and warrant further study. Zhou and Xie (2018) serves as a useful comparison point for our results as their model differs only in the lower boundary condition and the choice of a gray radiation scheme.

Despite the extensive research highlighted above, fundamental questions persist about the theoretical basis of monsoon formation. The complications introduced by zonally confined continental geometry, land surface moisture constraints, and albedo contrasts have yet to be fully elucidated (e.g. Zhai and Boos 2015; Maroon and Frierson 2016; Zhou and Xie 2018; Levine and Boos 2017). The chief purpose of this study is to determine the key mechanisms of monsoon formation across a broad range of climate conditions. The analysis focuses on the processes driving seasonal precipitation that would be relevant beyond the idealized model setting. Motivated by a recent work (Smyth and Ming 2020), we take the summer circulation over South American continental geometry as our focal point, but the analysis aims to elucidate the dynamics of a generic, deep tropical monsoon. In an idealized framework, the experiments map the parameter space of land albedo and moisture conditions, with implications for the stages of seasonal monsoon development as well as the range of global monsoons with their diverse geographic and ecological settings. The holistic approach draws on numerous relevant theories and suggests some general principles regulating monsoon strength. Section 2 describes the idealized moist GCM and the suite of experiments.

128 Section 3a presents the results for varying land moisture conditions, Section 3b is an MSE budget  
129 analysis, and Section 3c examines the land albedo perturbation experiments. Section 4 provides  
130 an overview of the monsoon formation mechanisms over the range of land surface conditions.

## 131 **2. Experimental Design**

132 We use an idealized moist general circulation model as described in Clark et al. (2018). The  
133 highly simplified atmospheric physics largely follows Frierson (2007), with the exception of re-  
134 placing the gray-atmosphere radiation with a full radiative transfer scheme, which makes it fea-  
135 sible to explicitly simulate water vapor feedbacks. The model includes a basic boundary layer  
136 parameterization and a simplified Betts-Miller (SBM) convection scheme with a default convec-  
137 tive relaxation timescale ( $\tau_{BM}$ ) of 2 hours. This timescale dictates how fast simulated profiles of  
138 temperature and humidity are relaxed to convectively adjusted reference states once certain criteria  
139 are met (Frierson 2007). The SBM scheme includes shallow, non-precipitating convection by re-  
140 laxing unstable temperature profiles to reference profiles, as well as deep, precipitating convection  
141 when moisture and temperature profiles exceed stability thresholds, including a 70% relative hu-  
142 midity criterion. Precipitation can also form on the grid scale by removing water vapor in excess  
143 of saturation. Neither parameterized convection nor grid-scale precipitation gives rise to clouds.  
144 Thus, cloud feedbacks, a major source of uncertainty in climate modeling, are excluded from the  
145 model. The CO<sub>2</sub> concentration is prescribed to 369.4 ppm, and CH<sub>4</sub> to 1.821 ppm. The experi-  
146 ments are run at T42 spectral resolution (64 latitude by 128 longitude gridpoints) with 30 vertical  
147 levels.

148 The lower boundary condition includes a slab mixed layer ocean with a heat capacity equal to  
149 20 meters of water and a prescribed, time-invariant meridional oceanic heat flux, and an isolated  
150 South American continent with 10% of the slab ocean heat capacity (i.e. 2 meters of water). The

151 South American continent has realistic geometry but no topography (i.e. completely flat), and  
152 does not include Central America. The exclusion of the Andes mountain range is notable given  
153 the attention placed on its climate significance in previous work. For example, the Andes act as a  
154 barrier shielding the continent from low MSE oceanic air (e.g. Garreaud and Aceituno 2001) and  
155 support low level jet formation both by diverting easterly winds and via lee cyclogenesis (Wang  
156 and Fu 2004). The choice of an isolated continent minimizes the broader climatic impact of land  
157 moisture and albedo perturbations by confining them to a comparatively small area, facilitating  
158 comparison between experiments. On the other hand, the realistic geometry enables more direct  
159 comparison of the monsoon sector with both observations and comprehensive model experiments,  
160 including the Geophysical Fluid Dynamics Laboratory (GFDL) AM4 simulations that motivate  
161 the present study (Smyth and Ming 2020).

162 A suite of experiments forced with a modern-day seasonal cycle of insolation is designed to  
163 elucidate the impact of land moisture and albedo conditions on monsoon characteristics. Though  
164 the present study focuses on the case of South America as a bridge to previous work, the use of an  
165 idealized model and the focus on mechanistic analysis should yield insights that inform our general  
166 understanding of monsoons. The three land moisture configurations include a “realistic” continent  
167 (R) with a bucket hydrology model governing potential evaporation, a “dry” (D) continent with  
168 zero evaporation, and a “wet” continent (W) in which the land is an infinite reservoir of moisture  
169 (i.e. the only distinction between land and ocean is in heat capacity). The bucket hydrology model  
170 (Manabe 1969) in the R configuration scales the potential evaporation based on a bucket capacity  
171 of 150 mm and a 0.75 saturation fraction, as in Vallis et al. (2018) and Clark et al. (2020). For each  
172 moisture condition, we perform six albedo perturbation experiments with land albedo prescribed to  
173 0.1, 0.26, 0.3, 0.4, 0.5, 0.7, and 1.0. Note that 0.26 is the default surface albedo over both land and  
174 ocean, and is chosen to attain a realistic climate in the absence of clouds (Frierson et al. 2006). The

name of an experiment contains a letter (denoting the moisture condition) followed by a number (denoting the albedo). For instance, R0.26 refers to the experiment in which one uses the bucket hydrology model and the default albedo of 0.26. To discern the effect of the convective relaxation time on the monsoon simulation, we examine three experiments in the R0.26 configuration with  $\tau_{BM}$  varied to 4, 8, and 16 hours, as in Clark et al. (2018). Each simulation is run for 20 years with the final 15 years of daily output used for analysis.

### 3. Results

#### *a. Varying land moisture conditions*

Irrespective of the local moisture availability in the idealized model simulations, the seasonal cycle over the South American monsoon sector ( $5-18^\circ$  S,  $40-72^\circ$  W) is distinctly monsoonal in all three experiments with the default surface albedo (0.26) (Fig. 1a). Modest precipitation commences in October, two to three months after surface temperatures ( $T_{surf}$ ) shift to a warming trajectory in late winter (Fig. 1b). With bucket hydrology (R0.26), a maximum rainfall rate of  $6.2 \text{ mm d}^{-1}$  occurs in February, and without a local moisture source (D0.26), the peak monthly mean rainfall of  $4.4 \text{ mm d}^{-1}$  occurs a month earlier, in January. When local moisture is unlimited (W0.26), rainfall maximizes at  $9.1 \text{ mm d}^{-1}$  in February. [Throughout the paper, the monsoon season refers to January to March (JFM), the period encompassing the highest mean rainfall rate.] In R0.26,  $T_{surf}$  decreases as precipitation intensifies in JFM because in a moisture-limited regime, latent heat fluxes can increase at the expense of sensible heat fluxes (e.g. Berg et al. 2015). In D0.26 and W0.26, this coupling is eliminated since the local moisture is externally controlled. This may partly explain why  $T_{surf}$  in the dry and wet cases is relatively flat during the monsoon season. In all experiments, precipitation rapidly retreats from April through June, and the dry sea-

son extends from July through September (JAS). During this time, there is virtually zero rainfall when local moisture fluxes are limited or disabled, while the mean precipitation hovers around 1 mm d<sup>-1</sup> in the W0.26 experiment (Fig. 1a). Insolation minimizes in June, and minimum surface temperatures lag this by one month in the R0.26 and D0.26 experiments and by two months in W0.26 (Fig. 1b). In D0.26, surface temperatures respond more strongly to the insolation forcing without the moderating effect of latent heat fluxes on the surface energy balance. The D0.26 experiment exhibits the lowest amplitude annual cycle of precipitation, but the most seasonal variation of surface temperature (13 K range, compared to 11 K in R0.26 and 8 K in W0.26).

From a net precipitation perspective ( $P - E$ ) (equivalent to the large-scale moisture convergence), the rainy season disparity between experiments is smaller, given the substantial enhancement of evaporation in the R and W experiments (Fig. 1c). Note that there is no land evaporation in the D experiment, so  $P - E$  is the same as  $P$ . The JFM mean  $P - E$  is very similar in D0.26 (4.2 mm d<sup>-1</sup>) and W0.26 (3.1 mm d<sup>-1</sup>), which underscores the prominent role of the large-scale circulation in importing moisture from the ocean in both extreme cases. By contrast, the  $P - E$  is lower in R0.26 (1.8 mm d<sup>-1</sup>). This indicates that the relationship between large-scale moisture convergence and local moisture conditions is non-monotonic in the rainy season; moisture convergence is higher with dry or saturated land than in the intermediate case. During the dry season, the disparity in  $P - E$  is greater than that in precipitation; the JAS mean  $P - E$  is negative in R0.26 (-0.33 mm d<sup>-1</sup>) and W0.26 (-2.6 mm d<sup>-1</sup>). In W0.26,  $P - E$  remains negative into the monsoon onset season (October through December, or OND) before increasing sharply. In the W0.26 simulation this continental region serves as a prominent net moisture source for much of the year, an unrealistic consequence of simulating land without a limit on potential evaporation. Nonetheless, the magnitude and phasing of the precipitation in W0.26 is remarkably similar to the observed 1997-2015 annual cycle from the Global Precipitation Climatology Project v2.3, especially from

221 January to August (Fig. 1a). In this model, a saturated land surface produces the most realistic  
222 seasonal cycle of precipitation over the monsoon sector, perhaps by best representing the strong  
223 evapotranspiration from vegetation in this region. In all three idealized model experiments the  
224 monsoon onset season precipitation is delayed and substantially weaker than observed, underlying  
225 a rather abrupt transition.

226 Despite the simplicity of the model configuration, especially in the absence of the Andes Moun-  
227 tains, the spatial distribution of monsoonal precipitation is largely consistent with observed pat-  
228 terns (Fig. 2), suggesting that the realistic geometry and the differing heat capacity of land and  
229 ocean are sufficient to induce a fairly realistic monsoonal climate in the presence of insolation  
230 forcing. The key discrepancy in the atmospheric circulation without the Andes is that low-level  
231 westerly flow from the tropical Pacific contributes to the continental moisture convergence (Fig.  
232 3). This westerly inflow is particularly strong in D0.26, where a cyclonic circulation on the west-  
233 ern continent produces a precipitation maximum near  $70^{\circ}$  W, with a relatively narrow rainfall band  
234 extending across the width of the monsoon sector (Fig. 3a). Precipitation exceeding  $4 \text{ mm d}^{-1}$   
235 extends from the east coast to  $60^{\circ}$  W in R0.26, with the strongest mean precipitation near  $40^{\circ}$   
236 W (Fig. 2b). When surface moisture is unlimited, the monsoon is coherent with the oceanic In-  
237 tertropical Convergence Zone (ITCZ) both west and east of the continent, though the precipitation  
238 has a broader southward extent over South America (Fig. 2c).

239 One notable feature in the simulations is the limited southeastward extension of the South At-  
240 lantic Convergence Zone (SACZ), a convective band that emanates from the Amazon basin over  
241 the South Atlantic Ocean. Previous work suggests that the SACZ forms when midlatitude fronts  
242 stall at longitudes with enhanced tropical convection and Rossby waves propagate equatorward  
243 (Nieto Ferreira and Chao 2013; Van Der Wiel et al. 2015). In a series of aquaplanet experiments,  
244 Nieto Ferreira and Chao (2013) find that an SACZ-like feature develops when a prescribed patch

245 of enhanced tropical convection attains sufficient strength and poleward extent. In line with Ko-  
246 dama (1992, 1993), they emphasize that strong poleward low-level flow on the eastern flank of the  
247 monsoon region, or along the west of the subtropical high, is crucial for moisture convergence and  
248 SACZ formation. The underdevelopment of the SACZ may be attributed to discrepancies in the  
249 location and intensity of such a low-level jet in the idealized simulations. In all three experiments,  
250 northerly flow on the eastern coast of the continent does not extend poleward of  $15^{\circ}\text{S}$  (Fig. 3).  
251 In R0.26 and W0.26, the winds have a northwesterly orientation and are relatively weak, possibly  
252 due to the weaker land-ocean thermal gradients.

253 Like the magnitude of the precipitation, the region-mean near-surface (973 hPa) JFM MSE  
254 increases with local moisture availability. The MSE or  $h$  is defined as  $h = c_p T + gz + L_v q - L_f q_{ice}$ ,  
255 where  $c_p$  is the heat capacity of air at constant pressure,  $T$  is temperature,  $g$  is the gravitational  
256 constant,  $z$  is geopotential height,  $L_v$  is the latent heat of vaporization of water, and  $q$  is specific  
257 humidity. In D0.26, the near-surface MSE is lower over the central monsoon sector than the  
258 surrounding coastal land, which is mirrored by the precipitation distribution (Fig. 2a). The MSE  
259 distribution is more uniform over land and ocean in R0.26 and W0.26 (Fig. 2b, c). In R0.26 the  
260 highest near-surface MSE contour bisects the maximum precipitation, and in W0.26, the near-  
261 surface MSE is highest just poleward of the strongest precipitation, consistent with CQE theory  
262 (Emanuel 1995; Privé and Plumb 2007a; Nie et al. 2010). In Section 3c we examine the extent to  
263 which the MSE distribution guides the precipitation when land albedo is varied (Hurley and Boos  
264 2013).

265 While each of these baseline experiments exhibits a monsoonal climate, the precipitation orig-  
266 inates via different pathways in the model. With dry land, all moisture for precipitation derives  
267 from oceanic regions, so the monsoon sector is particularly reliant on easterly and westerly inflow  
268 of moist air from the tropical ocean. With unlimited moisture, the mean JFM evaporation rate is

60% of the precipitation rate, which points to the substantial local moisture recycling evident from the  $P - E$  results. Additionally, in D0.26, the rainy season precipitation ( $4.2 \text{ mm d}^{-1}$ ) derives almost exclusively from large-scale processes, with precipitation occurring when an entire grid box reaches saturation (Fig. 2a). By contrast, in the R0.26 ( $5.3 \text{ mm d}^{-1}$ ) and W0.26 ( $7.8 \text{ mm d}^{-1}$ ) experiments, JFM precipitation is largely produced by the parameterized Betts-Miller convection scheme (88% and 96%, respectively). Given the 70% relative humidity threshold in the SBM convection scheme, the ratio of large-scale to convective rainfall strongly depends on the near-surface humidity (Frierson 2007), a point to which we will return.

The underlying large-scale circulation characteristics differ markedly across the range of land moisture conditions. The mean ascent profiles in the R0.26 and W0.26 experiments indicate top-heavy moist convection that penetrates the upper troposphere, with vertical velocity maxima ( $50$  and  $70 \text{ hPa d}^{-1}$ , respectively) at approximately  $400 \text{ hPa}$  (Fig. 4a). The dry land case is characteristic of a shallow overturning circulation with vigorous ascent; the maximum vertical pressure velocity ( $\omega$ ) is  $120 \text{ hPa d}^{-1}$  at  $750 \text{ hPa}$  (Fig. 4a). Though the ascent profile is relatively shallow, weaker ascent does penetrate to  $250 \text{ hPa}$ . The region-mean MSE profiles also reflect the differing nature of the monsoon across moisture conditions (Fig. 4b). Although MSE decreases with height in the lower troposphere in all cases before starting to increase, the location of the MSE minimum becomes progressively lower with the increasing availability of moisture. Note that the observed tropical MSE profile typically shows a minimum in the mid-troposphere (around  $600 \text{ hPa}$ ) (Back and Bretherton 2006). A possible reason is that the free troposphere in the idealized simulations is biased dry, presumably due to the absence of moistening through convective detrainment of cloud condensates. The R0.26 and W0.26 profiles are firmly under convective quasi-equilibrium (CQE) control, with precipitation produced primarily via the simplified Betts-Miller (SBM) convection scheme. It seems questionable whether this is the case for D0.26, in which the parameterized con-

vection ceases to operate and precipitation is produced exclusively through large-scale processes. The comparably low near-surface MSE in D0.26 demonstrates the strong effect of local moisture limitations on the overlying atmosphere. Nonetheless, the upper-tropospheric MSE is approximately equal to the near-surface MSE near an altitude of 200 hPa in D0.26, in a way similar to the other two cases (Fig. 4b). This indicates that the resolved (grid-scale) convection, albeit pathological, still plays a role in establishing this linkage between near-surface and upper-tropospheric MSE.

The impact of varying land moisture availability is also evident in the vertical distributions of several other key variables. The dry static energy (DSE) profiles reflect hotter near-surface conditions in the D0.26 experiment as well as a much deeper boundary layer in which quasi-conserved quantities such as DSE are relatively well-mixed (Fig. 4c). This homogenization occurs partly via non-precipitating (dry), shallow convection in the SBM convection scheme (Frierson 2007). Near-surface DSE is highest in the D0.26 experiment and lowest in the W0.26 experiment. By contrast, in the upper troposphere, DSE is highest in the W0.26 experiment and lowest in the D0.26 experiment. As this part of the atmosphere is devoid of moisture (i.e. similar DSE and MSE), it means that the increased availability of land moisture leads to a warming of the upper troposphere. This is a manifestation of the relative standing in near-surface MSE across the experiments which impacts the upper troposphere through convection.

The vertical distribution of specific humidity ( $q$ ) also varies in these experiments. D0.26 has a much drier boundary layer than R0.26 and W0.26. In all cases, relatively high near-surface moisture values fall off sharply with height at least partly owing to the missing convective detrainment, reducing tropospheric relative humidity values (Fig. 4d,e). Consistent with these temperature and moisture distributions, the D0.26 experiment has arid near-surface conditions with 25% mean relative humidity (RH) compared to 60% and 70% RH in the R0.26 and W0.26 experiments,

317 respectively (Fig. 4e), which are sufficiently close to the SBM convective threshold (70%). By  
318 contrast, it is far too dry for convective precipitation in D0.26. The precipitation intensity distri-  
319 butions also reflect this; in W0.26 the daily rainfall distribution is spread broadly over the 0 to 20  
320 mm d<sup>-1</sup> range due to frequent moist convection (not shown). In D0.26 by contrast, the distribution  
321 has a long tail of infrequent extreme rain events (produced by large-scale scheme), while on the  
322 majority of days there is near-zero rainfall.

323 It is interesting to think about what controls the upper-tropospheric MSE in these experiments.  
324 In the weak temperature gradient (WTG)/CQE framework (e.g. Byrne and O’Gorman 2013; Hill  
325 et al. 2017; Zhang and Fueglistaler 2020), the upper-tropospheric MSE is dictated by the highest  
326 near-surface MSE. Fig. 5 shows that the highest near-surface MSE is located either over the land  
327 monsoon region or over the neighboring ocean. There is an inherent land-sea temperature contrast  
328 due to a combination of reduced mixed layer depth and limited moisture. The land warming un-  
329 avoidably spills across the land-sea boundary, causing the adjacent ocean to be warmer than the  
330 remote ocean. Given that the oceanic boundary layer is close to saturation, higher temperature  
331 translates to higher MSE. This means that the upper-tropospheric MSE in the three simulations is  
332 controlled locally by the broadly defined monsoon region (land and adjacent ocean). This conclu-  
333 sion is consistent with Fig. 4b, which shows that the near-surface and upper-tropospheric MSE is  
334 tightly connected. The near-surface MSE maximum at continental longitudes draws the precipita-  
335 tion southward (Fig. 5), in accordance with the CQE framework.

## 336 *b. MSE Budget Analysis*

337 The region-mean MSE budget analysis further illustrates the differing character of the mon-  
338 soonal circulation in the experiments. The column-integrated MSE budget is given by:

$$\frac{\partial}{\partial t}\{\overline{\mathcal{E}}\} + \{\bar{\mathbf{v}} \cdot \nabla_p \bar{h}\} + \left\{ \bar{\omega} \frac{\partial \bar{h}}{\partial p} \right\} + \nabla \cdot \{\bar{h}' \bar{\mathbf{v}}'\} \approx \bar{F}_{net}, \quad (1)$$

339 wherein brackets denote mass-weighted column integrals, overbars are time means, primes are  
340 temporal deviations,  $\mathcal{E}$  is the internal energy,  $\mathbf{v}$  is the horizontal wind vector,  $\nabla_p$  is the horizontal  
341 gradient operator on constant pressure surfaces,  $\omega$  is vertical velocity in pressure coordinates, and  
342  $\bar{F}_{net}$  is the net column energy.  $\bar{F}_{net}$  is the sum of top-of-atmosphere (TOA) and surface radiative  
343 fluxes into the column plus the surface turbulent fluxes.

344 Based on a calculation of the region mean column-integrated MSE budget (Table 1) following  
345 Hill et al. (2017), the vertical MSE advection is negative in the D0.26 experiment, denoting energy  
346 import by the circulation, and positive in the R0.26 and W0.26 experiments. In all three cases, the  
347 DSE component of the vertical MSE advection term is positive, since DSE increases with altitude,  
348 while the moisture component is negative. Only in the D0.26 experiment does the latter dominate.  
349 Between 600 and 800 hPa the vertical moisture gradient, decreasing with altitude, is sampled by  
350 very strong vertical velocity values.

351 The negative  $\left\{ \bar{\omega} \frac{\partial \bar{h}}{\partial p} \right\}$  in D0.26 corresponds to a negative gross moist stability (GMS). The GMS  
352 relates the column energy transport to the strength of the mean circulation and can be thought of  
353 as the efficiency of a circulation's energy export (Bretherton et al. 2006). It is determined by the  
354 structure and amplitude of the vertical velocity, along with the stratification of the MSE. In this  
355 sense, the D0.26 monsoon circulation is similar in nature to the observed East Pacific ITCZ, a  
356 region of relatively shallow precipitating convection with a negative GMS (Back and Bretherton  
357 2006). By contrast, the monsoon dynamics in R0.26 and W0.26 resemble the deep convection

of the West Pacific ITCZ, with positive vertical MSE advection values denoting energy export. These circulations comply with the Neelin and Held (1987) theory of tropical rainfall in which vertical MSE advection plays a chief role in balancing column heating, and precipitating tropical convection is associated with a positive GMS.

The horizontal MSE advection term is similar across the three experiments, between 5 and 10  $\text{W m}^{-2}$ , and contributes to MSE export in each case. A decomposition of the horizontal MSE advection into dry and moist components, however, reflects differences between the experiments. In D0.26, the advection of relatively cool, moist air from the adjacent ocean produces a positive horizontal DSE advection ( $\{\bar{\mathbf{v}} \cdot \nabla_p \overline{DSE}\} = 39.2 \text{ W m}^{-2}$ ) and a negative column horizontal moisture advection ( $\{\bar{\mathbf{v}} \cdot \nabla_p \overline{L_v q}\} = -33.7 \text{ W m}^{-2}$ ). In the R0.26 and W0.26 configurations, the region mean horizontal DSE advection is near zero (2.4 and -0.1  $\text{W m}^{-2}$ ), while the horizontal moisture advection is positive, denoting export (7.8 and 6.4  $\text{W m}^{-2}$ ). These results indicate a relatively small land-sea temperature contrast and higher specific humidity over land than over ocean.  $F_{net}$  differs by an order of magnitude between the experiments, ranging from 7.8  $\text{W m}^{-2}$  in D0.26 to 64  $\text{W m}^{-2}$  in W0.26. This is due primarily to differences in outgoing longwave radiation (OLR), with higher surface temperatures and thus OLR over dry land. The impact of the net column energy flux on the regional climate is examined further in the analysis of the albedo perturbation experiments.

The budget analysis demonstrates that in all three baseline experiments, precipitation is generated by the mean flow rather than transients. Mean ascent in the monsoon sector drives moisture convergence and precipitation, while transient eddies diverge moisture. The MSE eddy flux divergence is dominated by the moisture contribution in all three experiments, and the DSE component is negative in R0.26 and W0.26, indicating DSE convergence over the monsoon sector. The predominance of the mean circulation in generating precipitation is further supported by an assessment of the vertical and horizontal shears of the zonal mean wind. The zonal flow is stable

382 according to the Charney-Stern criterion for baroclinic instability, with a positive meridional po-  
383 tential vorticity gradient across the monsoon domain (not shown) (Charney and Stern 1962; Hsieh  
384 and Cook 2005).

385 *c. Land albedo perturbation experiments*

386 To better understand the impact of net column energy fluxes on monsoon characteristics, as  
387 well as the limits of monsoonal climate regimes, we examine a suite of land albedo perturbation  
388 experiments. Land albedo variations drastically impact the monsoonal precipitation magnitude  
389 (Fig. 6), in agreement with previous studies (Zhou and Xie 2018; Boos and Storelvmo 2016).  
390 With all three moisture conditions, JFM precipitation declines monotonically with increasing land  
391 albedo, with minimal rainfall at albedo values of 0.5 or higher. Regardless of local moisture  
392 availability, when the albedo is increased to 0.7 or 1.0, the monsoon region is subject to mean  
393 descent throughout the atmospheric column (Fig. 7).

394 The surface temperatures over land in the R0.5 and D0.5 experiments (296 K and 301 K, re-  
395 spectively) remain higher than adjacent SSTs, so that a weak, viscously driven circulation persists,  
396 though it produces negligible precipitation (Fig. 7a, b). In the R and D experimental suites, ascent  
397 is confined to the boundary layer when albedo values are prescribed to 0.4 or 0.5 (Fig. 7a,b). In  
398 these simulations, the surface temperature distributions induce low-level pressure gradients which  
399 drive convergence over the monsoon sector. In the lower range of land albedo values, the R and  
400 D experiments diverge. In the D0.3, D0.26, and D0.1 experiments, the ascent grows increasingly  
401 vigorous and vertically extended. While the ascent maximum is relatively low in each of these  
402 experiments (below 650 hPa), the ascending motion extends through the mid-troposphere, and is  
403 accompanied by a jump in precipitation intensity with mean values of 3.4, 4.2, and 6.9 mm d<sup>-1</sup>,  
404 respectively, compared to 1.3 mm d<sup>-1</sup> in the D0.4 experiment. Even when land albedo is lowered

405 to 0.1 in the dry land configuration, the precipitation derives almost exclusively from the large-  
406 scale scheme. By contrast, in the R0.3, R0.26, and R0.1 experiments, deep convection develops  
407 and precipitation increases to 3.7, 5.3, and 9.1 mm d<sup>-1</sup>, respectively. The shape of the ascent  
408 profiles and the proportion of convective to total precipitation support that convective instability  
409 underlies the monsoon development in these experiments.

410 In the wet land configuration, land albedo variations do not alter the precipitation mode; in any  
411 experiment in which land remains thermodynamically favorable, precipitation is driven almost  
412 exclusively by convective instability. In W0.1 the vertical velocity profile strengthens, and when  
413 the land albedo is increased to 0.3 or 0.4, convection weakens but remains vertically extensive  
414 (Fig.7c). In the W0.5 experiment, without land-ocean gradients in surface moisture availability,  
415 the albedo perturbation reduces the temperature of land to 290 K, below that of the nearby sea  
416 surface, resulting in mean descent through the column (Fig. 7c). Boundary-layer confined ascent  
417 only develops in the simulations with land moisture limitations.

418 We consider the hypothesis that inertial instability underlies the enhancement of the monsoonal  
419 circulation in the three dry low-albedo experiments (i.e. D0.3, D0.26, and D0.1) (Plumb and Hou  
420 1992; Tomas and Webster 1997). The near-surface (920 hPa) absolute vorticity ( $\eta$ ) distribution  
421 supports this, as the zone of locally anticyclonic absolute vorticity expands with the off-equatorial  
422 migration of the  $\eta = 0$  contour over continental latitudes when albedo is reduced below 0.4 (Fig.  
423 8a, b). In inertially unstable zones, the divergent wind accelerates to generate a locally cyclonic  
424 tendency term, relaxing the instability. The resulting convergence zone intensifies local convec-  
425 tion and precipitation. In the three low-albedo experiments, the near-surface divergence over the  
426 central continent is predominantly equatorward of  $\eta = 0$ , with the convergence zone largely lying  
427 poleward thereof, consistent with Tomas and Webster (1997) (Fig. 8a, b). This is not the case  
428 in the higher albedo experiments, including D0.4 and D0.5, in which the continental convergence

zone straddles the  $\eta = 0$  contour which hovers closer to the equator (Fig. 8c, d). Furthermore, the highest 920 hPa divergent wind speeds are bisected by the  $\eta = 0$  contour when it deviates poleward over the continent in the D0.3, D0.26, and D0.1 experiments (not shown). In D0.4 and D0.5, the maximum divergent wind speeds over continental longitudes occur north of the equator.

In the R and W experimental suites, inertial instability seems to play a less central role in monsoon development. In February, the  $\eta = 0$  contour migrates only slightly further poleward over the continent than over the adjacent ocean, and the displacement is smaller than in the dry land experiments (not shown). For example, in D0.26, the maximum southward displacement of the contour over the continent is  $4.2^\circ$ , compared to  $2.4^\circ$  in the R0.26 experiment and  $2.7^\circ$  in W0.26. This disparity may be explained by the relatively strong cross-equatorial pressure gradient in the dry land experiments caused by the particularly strong heating of the continent.

In terms of the spatial distribution of precipitation, the effect of albedo variations depends on the land moisture configurations (not shown). In the D configuration, the near-surface MSE maximum does not shift substantially in response to albedo perturbations. Correspondingly, there is little latitudinal change in the monsoon location. At lower albedo values in the W configuration, and to a lesser extent in R, the near-surface MSE maximum increases and shifts poleward, and the monsoon expands poleward, in accordance with CQE predictions (Hurley and Boos 2013). In both the R and W experiments, JFM precipitation is strongest near the Atlantic coast, and as the continent heats up at lower albedo values, the monsoon penetrates further westward over the continent. Increased continental heating and thermal gradients can enhance baroclinicity of prevailing easterlies and thus convective storm formation, driving a westward expansion of the monsoon; such a process underlies the strengthening of African Easterly Wave activity in global warming simulations (Skinner and Diffenbaugh 2014). The spatial pattern of precipitation differs in the D suite; a local precipitation maximum near the west coast, coinciding with a local MSE maximum, emerges

when the land albedo is 0.3 or lower. The thermal low over the continent induces convergence of westerly winds from the Pacific and easterly winds from the Atlantic. These lower-tropospheric winds are stronger in the D suite than the corresponding R and W experiments due to the relatively strong land-sea thermal contrast (Fig. 3). With realistic topography, this moist westerly inflow would be impeded by the Andes.

When land surface albedo is varied across a broad range, various types of monsoonal circulations arise. At the highest albedo values, the land surface is cooler than the zonal mean value and the monsoon vanishes. At moderate albedo values, a viscously driven circulation emerges in local summer, producing a modest seasonal cycle of precipitation over off-equatorial South America. When albedo is reduced to 0.4 or below, inertial instability triggers enhanced convergence and precipitation in the dry land experiments, while convective instability produces more substantial rainfall in the realistic and wet land configurations. Even when the land albedo is suppressed to 0.1, the absence of latent heat fluxes leads to an exceedingly dry boundary layer and inhibits parameterized moist convection in the dry land experiment. It is notable that even without parameterized convection, the JFM precipitation in D0.1 is substantial ( $6.9 \text{ mm d}^{-1}$ ) and exceeded only by the W0.26, W0.1, and R0.1 experiments ( $7.8, 12.2, 9.1 \text{ mm d}^{-1}$ , respectively). When  $F_{net}$  is sufficiently strong, moisture transport and convergence partially compensate for the disabling of local moisture recycling. Evidently, while a local moisture limitation shapes the monsoonal regime, this parameter alone does not impede the monsoon's emergence nor its intensification. This has implications for monsoon onset, which occurs when local moisture availability is constrained following the dry season in South America. Throughout the spring, increasing local soil moisture and latent heat fluxes enable the vigorous convection of the monsoon season (Fu and Li 2004). The processes driving the initial precipitation that primes the region for monsoon development may resemble the mechanisms in the D suite.

477     Regardless of the physics underlying precipitation development across the suite of experiments,  
478     the JFM precipitation increases nearly linearly with  $F_{net}$ , suggesting that this is a key parameter  
479     modulating monsoon intensity (Fig. 9a). Moderate precipitation develops only when  $F_{net}$  values  
480     exceed zero. While local moisture conditions circumscribe the physical triggers of convection, in  
481     any case the magnitude of the precipitation is related to the magnitude of the MSE flux divergence.  
482     The circulation must comply with the moist static energy budget, meaning the MSE flux diver-  
483     gence by the total circulation (horizontal advection, vertical advection and eddies) must balance  
484     the net forcing and the time tendency (the latter changes negligibly). A higher net column forcing  
485     necessitates a stronger mean circulation and/or more pronounced MSE gradients on which the cir-  
486     culation acts. In the dry land experimental suite, the circulation strength (using vertical pressure  
487     velocity as a proxy) increases drastically as albedo is reduced, supporting more moisture import  
488     and stronger convergence (Fig. 7a). In the experiments with higher land moisture availability, the  
489     circulation strength also increases with the net column forcing, albeit more modestly. In each suite  
490     of experiments, there is a concomitant enhancement of precipitation. This relationship between  
491     precipitation and net column forcing aligns with the findings of Boos and Storelvmo (2016), who  
492     demonstrate that monsoon strength has a nearly linear dependence on radiative forcing in both a  
493     comprehensive GCM and an analytical model.

494     Examining the TOA components of the net forcing term, the relationship between precipitation  
495     and net shortwave radiation is more consistent among experiments than the relationship between  
496     precipitation and OLR (not shown). As described earlier, the OLR is consistently higher in the dry  
497     land experiments due to the restrictions imposed on the land surface energy budget. By the same  
498     reasoning, the region-mean OLR at a given precipitation rate is consistently lower in the wet land  
499     experiments than the R experiments.

500 To better compare thermodynamic conditions given these moisture-modulated differences in the  
 501 surface energy budget, we examine the relationship between near-surface  $\theta_e$  and precipitation. In  
 502 all three configurations, as albedo decreases, precipitation increases accompany increases in both  
 503 the continental near-surface MSE and its horizontal gradient. This underscores that a positive  
 504 relationship between the amplitude of precipitation and near-surface MSE can persist even when  
 505 parameterized convection is largely inactive (Fig. 9b). As the contrast between the monsoon-sector  
 506 MSE and the tropical mean value increases, the magnitude of monsoonal precipitation increases  
 507 (not shown), consistent with the CQE framework for precipitation. Figure 9b illustrates a thresh-  
 508 old behavior: all experiments with region-mean  $\theta_e$  below 302 K have negligible precipitation. In  
 509 the remaining experiments, in which region-mean  $\theta_e$  values range from 306 K to 313 K, precip-  
 510 itation steadily increases with  $\theta_e$  regardless of the land moisture condition. It is striking that this  
 511 relationship holds in the dry land experiments, given the impedance of parameterized convection  
 512 and the expectation that this would disrupt CQE conditions in the atmosphere as in Zhou and Xie  
 513 (2018).

## 514 **4. Discussion**

515 The suite of idealized model experiments demonstrates the profound impact of land surface con-  
 516 ditions on monsoon dynamics. These experiments, and the precipitation mechanisms they reveal,  
 517 may inform our understanding of the stages of monsoon development on Earth. As an example,  
 518 we consider the seasonal cycle over the South American monsoon sector as simulated in the GFDL  
 519 AM4 model with prescribed climatological SSTs. In previous work, the authors examined the sea-  
 520 sonally varying responses of precipitation in the South American monsoon sector to uniform 2-K  
 521 SST warming in the GFDL AM4 model (Smyth and Ming 2020). Though the spring and fall are  
 522 both characterized by moderate precipitation rates and similar region-mean MSE budget regimes

in AM4, they exhibit different responses to warming. Spring rainfall decreases by 11% and  $P - E$  decreases by 40%, while fall rainfall remains unchanged. This difference is linked to the difference in the climatological low-level relative humidity, which is 60% in spring and 80% in fall. The seasonal contrast in RH impacts the surface temperature and boundary layer MSE distributions and leads to different anomalous patterns in the SST warming experiment. Ultimately, the more pronounced land-sea contrast in spring renders the season vulnerable to drying by anomalous horizontal MSE advection in the +2-K experiment. The study concludes that differing boundary layer humidity plays a crucial role in setting the monsoon properties and thus the sensitivity to perturbations. This echoes Byrne and O’Gorman (2015), who find that changes in the horizontal gradients of temperature and fractional changes in relative humidity explain why the  $P - E$  response over land deviates from the canonical wet-get-wetter scaling. To what extent can the idealized model results shed light on these findings?

To assess whether the linear relationship between net column heating and precipitation holds beyond the idealized modeling framework, Figure 9a includes the data points for the four seasons in AM4 control and +2-K experiments. The seasonal cycle in AM4 exhibits hysteresis in this parameter space (Fig. 9a). In SON, preceding the rainy season, the AM4 control net column heating is  $69.5 \text{ W m}^{-2}$  and the precipitation rate is  $4.1 \text{ mm d}^{-1}$ . Following the rainy season, in MAM, the net column heating is lower ( $42.5 \text{ W m}^{-2}$ ) while the precipitation rate is higher ( $6.9 \text{ mm d}^{-1}$ ). As noted above, the shoulder seasons have similar MSE budget regulation regimes, as characterized by the relative strength of vertical to horizontal MSE advection (Smyth and Ming 2020). Mapping the seasonal cycle in Figure 9a points to the impact of the differing surface moisture availability on the efficiency of precipitation production. SON exhibits a clear deviation from the largely linear relationship across the idealized experiments and the other AM4 seasons (Fig. 9a). Based on net column heating, AM4 SON is most similar to W0.26 ( $F_{net} = 64.3 \text{ W m}^{-2}$ ),

547 but the W0.26 rainfall is nearly twice as strong ( $7.84 \text{ mm d}^{-1}$ ). When land surface moisture is  
 548 limited, substantial moisture convergence from the ocean is needed to produce rainfall. In SON,  
 549 the land heating is less pronounced than in the D suite and the circulation is substantially weaker,  
 550 while the dry soil remains a limiting factor in generating precipitation.

551 The idealized experiments also exhibit seasonal hysteresis in the relationship between  $F_{net}$  and  
 552 precipitation, despite the fact that land surface moisture is externally controlled in D0.26 and  
 553 W0.26. The seasonal cycle for D0.26 resembles that in AM4, though with reduced seasonal vari-  
 554 ability along both axes (Fig. 9a). This implies that the asymmetry between monsoon onset and  
 555 withdrawal is due to the nature of the circulation, and is not entirely a consequence of seasonally  
 556 varying land surface moisture availability. Though  $F_{net}$  decreases strongly from summer to fall,  
 557 even dropping below zero in D0.26, the circulation persists and continues to support relatively  
 558 high precipitation rates. Monsoon withdrawal follows an equatorward and off-continental shift  
 559 of near-surface MSE and temperature maxima (not shown). Figure 9b includes data for all four  
 560 seasons of the D0.26, R0.26, and W0.26 experiments, and demonstrates a consistent relationship  
 561 between near-surface  $\theta_e$  and precipitation throughout the seasonal cycle. While the net column  
 562 heating varies directly with the strength of the summer monsoonal circulation, the near-surface  $\theta_e$   
 563 is a better guide for capturing the monsoon-sector precipitation variability across seasons. This  
 564 again underscores the primacy of CQE.

565 The discrepancy between the monsoon onset season in AM4 (SON) and the idealized experi-  
 566 ments is likely linked to the absence of one or more key processes from the idealized configuration.  
 567 Connections between the idealized model simulations and AM4, or reality, must be drawn cau-  
 568 tiously given the drastic simplification of the climate in the idealized experiments. The absence  
 569 of global continental geometry impacts the general circulation in the idealized experiments, and  
 570 much of the physics is greatly simplified. In particular, the effects of clouds on surface tempera-

ture, radiative fluxes (and thus  $F_{net}$ ), and precipitation generation are noteworthy. Clouds might, for example, reduce surface temperatures over land and impede circulation strength in AM4 SON as compared to the idealized simulations with limited land moisture (eg. Sharma et al. 1998).

The conclusions are largely robust to variations in the convective relaxation timescale, except that the ratio of large-scale to convective rainfall depends strongly on this parameter. In the R0.26  $\tau_{BM}$  experiments, the percentage of precipitation deriving from the SBM scheme is 88% in the control ( $\tau_{BM} = 2$  h), 81% with  $\tau_{BM} = 4$  h, 71% with  $\tau_{BM} = 8$  h, and only 36% when  $\tau_{BM} = 16$  h. As expected, the near-surface relative humidity increases with the relaxation time, since the moisture profiles are less frequently relaxed via the convection scheme. The climate is otherwise robust to  $\tau_{BM}$ , which has no notable impact on the total precipitation, nor on the region-mean surface temperature, OLR, net column energy flux, or moisture convergence ( $P - E$ ).

Figure 10 provides a schematic overview of the monsoonal properties and relevant mechanisms as land surface conditions are varied. At the highest land albedo values, a monsoon cannot develop regardless of the land moisture condition, resulting in mean descent. Over dry land at mid-range land albedo values, a very shallow thermally driven monsoon develops. As land albedo decreases further, increasing the net column forcing and the cross-equatorial near-surface pressure gradient, inertial instability develops and leads to a deeper overturning cell. Deep convection can only develop when the land moisture constraint is relaxed, allowing latent heat fluxes to trigger convective instability. It is worthwhile to note that the shallow, thermally driven circulations resemble the regime described by Lindzen and Nigam (1987) in which boundary layer momentum dynamics play a crucial role. This view is supported by a set of perturbation experiments showing that increased land surface roughness enhances precipitation significantly in D0.26, and to a much lesser extent in R0.26 and W0.26.

594 The mechanisms at play in the idealized model simulations as land properties are modified  
595 may be relevant for the seasonal development of monsoons on Earth. Inertial instability alone  
596 is sufficient for producing a shallow but vigorous circulation and converging a large amount of  
597 moisture from the ocean. This mechanism may be key to monsoon onset following the dry season  
598 when soil moisture is low. Once the land is sufficiently moist, convective instability takes hold; the  
599 shallow circulation turns into a deep one. This mechanistic sequence is consistent with previous  
600 arguments (e.g. Fu et al. 1999) that wet season South American precipitation develops only after  
601 sufficient low-level moisture convergence reduces the convective inhibition.

602 In addition to elucidating the seasonal evolution of monsoon circulations, the idealized exper-  
603 iments indicate bounds on the range of land surface conditions that might support a monsoonal  
604 climate. When the net forcing is negative or the near-surface MSE is low, a monsoon does not  
605 develop. It will be interesting to evaluate such threshold behavior in more realistic modeling set-  
606 tings. This can illuminate historical changes in tropical hydroclimate and provides a basis for  
607 understanding the how rising carbon dioxide levels may impact monsoons via their effect on land  
608 surface conditions.

609 *Acknowledgments.* Thanks to Spencer Clark for his help running the idealized moist model. We  
610 also thank Spencer Hill and Spencer Clark, developers of the “aospy” climate model analysis  
611 package for Python. When published, model output will be made available at [osf.io](https://osf.io).

## 612 **References**

613 An, Z., and Coauthors, 2015: Global monsoon dynamics and climate change. *Annual Review of*  
614 *Earth and Planetary Sciences*, **43**, 29–77.

Back, L., and C. Bretherton, 2006: Geographic variability in the export of moist static energy and vertical motion profiles in the tropical pacific. *Geophysical research letters*, **33** (17).

Berg, A., B. Lintner, K. Findell, S. Seneviratne, and B. van den Hurk et al., 2015: Interannual coupling between summertime surface temperature and precipitation over land: Processes and implications for climate change. *J. Climate*, **28**, 1308–1328.

Bischoff, T., and T. Schneider, 2014: Energetic constraints on the position of the intertropical convergence zone. *Journal of Climate*, **27** (13), 4937–4951.

Boos, W. R., and T. Storelvmo, 2016: Near-linear response of mean monsoon strength to a broad range of radiative forcings. *Proceedings of the National Academy of Sciences*, **113** (6), 1510–1515.

Bordoni, S., and T. Schneider, 2008: Monsoons as eddy-mediated regime transitions of the tropical overturning circulation. *Nature Geoscience*, **1** (8), 515–519.

Bretherton, C. S., P. N. Blossey, and M. E. Peters, 2006: Interpretation of simple and cloud-resolving simulations of moist convection–radiation interaction with a mock-walker circulation. *Theoretical and Computational Fluid Dynamics*, **20** (5-6), 421–442.

Byrne, M. P., and P. A. O’Gorman, 2013: Land–ocean warming contrast over a wide range of climates: convective quasi-equilibrium theory and idealized simulations. *Journal of Climate*, **26** (12), 4000–4016.

Byrne, M. P., and P. A. O’Gorman, 2015: The response of precipitation minus evapotranspiration to climate warming: Why the “wet-get-wetter, dry-get-drier” scaling does not hold over land. *Journal of Climate*, **28** (20), 8078–8092, doi:10.1175/JCLI-D-15-0369.1.

- Chao, W. C., and B. Chen, 2001: The origin of monsoons. *Journal of the Atmospheric Sciences*, **58 (22)**, 3497–3507.
- Charney, J. G., 1975: Dynamics of deserts and drought in the sahel. *Quarterly Journal of the Royal Meteorological Society*, **101 (428)**, 193–202.
- Charney, J. G., and M. Stern, 1962: On the stability of internal baroclinic jets in a rotating atmosphere. *Journal of the Atmospheric Sciences*, **19 (2)**, 159–172.
- Chou, C., and J. D. Neelin, 2001: Mechanisms limiting the southward extent of the south american summer monsoon. *Geophysical research letters*, **28 (12)**, 2433–2436.
- Chou, C., and J. D. Neelin, 2004: Mechanisms of global warming impacts on regional tropical precipitation. *Journal of Climate*, **17 (13)**, 2688–2701.
- Clark, S. K., Y. Ming, and Á. F. Adames, 2020: Monsoon low pressure system–like variability in an idealized moist model. *Journal of Climate*, **33 (6)**, 2051–2074.
- Clark, S. K., Y. Ming, I. M. Held, and P. J. Phillipps, 2018: The role of the water vapor feedback in the itcz response to hemispherically asymmetric forcings. *Journal of Climate*, **31 (9)**, 3659–3678.
- Emanuel, K. A., 1995: On thermally direct circulations in moist atmospheres. *Journal of the atmospheric sciences*, **52 (9)**, 1529–1534.
- Emanuel, K. A. J. D. N., and C. S. Bretherton, 1994: On large-scale circulations in convecting atmospheres. *Quarterly Journal of the Royal Meteorological Society*, **120 (519)**, 1111–1143.
- Frierson, D., 2007: The dynamics of idealized convection schemes and their effect on the zonally averaged tropical circulation. *Journal of the Atmos. Sciences*, **64**, 1959–1975.

657 Frierson, D. M., I. M. Held, and P. Zurita-Gotor, 2006: A gray-radiation aquaplanet moist gcm.  
658 part i: Static stability and eddy scale. *Journal of the atmospheric sciences*, **63** (10), 2548–2566.

659 Fu, R., and W. Li, 2004: The influence of the land surface on the transition from dry to  
660 wet season in amazonia. *Theoretical and Applied Climatology*, **78** (1), 97–110, doi:10.1007/  
661 s00704-004-0046-7.

662 Fu, R., B. Zhu, and R. E. Dickinson, 1999: How do atmosphere and land surface influence seasonal  
663 changes of convection in the tropical amazon? *Journal of Climate*, **12** (5), 1306–1321.

664 Garreaud, R., and P. Aceituno, 2001: Interannual rainfall variability over the south american alti-  
665 plano. *Journal of climate*, **14** (12), 2779–2789.

666 Geen, R., S. Bordoni, D. S. Battisti, and K. Hui, 2020: Monsoons, itczs and the concept of the  
667 global monsoon. *Reviews of Geophysics*, e2020RG000700.

668 Hill, S. A., 2019: Theories for past and future monsoon rainfall changes. *Journal of Climate*, **5** (3),  
669 160–171.

670 Hill, S. A., Y. Ming, I. M. Held, and M. Zhao, 2017: A moist static energy budget–based analysis  
671 of the sahel rainfall response to uniform oceanic warming. *Journal of Climate*, **30** (15), 5637–  
672 5660.

673 Hsieh, J., and K. H. Cook, 2005: Generation of african easterly wave disturbances: Relationship  
674 to the african easterly jet. *Mon. Wea. Rev.*, **133**, 1311–1327.

675 Hurley, J., and W. Boos, 2013: Interannual variability of monsoon precipitation and local subcloud  
676 equivalent potential temperature. *Journal of Climate*, **26** (23), 9507–9527.

677 Kang, S., I. Held, D. Frierson, and M. Zhao, 2008: The response of the itcz to extratropical  
678 thermal forcing: Idealized slab-ocean experiments with a gcm. *Journal of Climate*, **21**, 3521–  
679 3532.

680 Kodama, Y., 1992: Large-scale common features of subtropical precipitation zones (the baiu  
681 frontal zone, the spcz, and the sacz) part i: Characteristics of subtropical frontal zones. *Journal*  
682 *of the Meteorological Society of Japan. Ser. II*, **70 (4)**, 813–836.

683 Kodama, Y.-M., 1993: Large-scale common features of sub-tropical convergence zones (the baiu  
684 frontal zone, the spcz, and the sacz) part ii: conditions of the circulations for generating the  
685 stczs. *Journal of the Meteorological Society of Japan. Ser. II*, **71 (5)**, 581–610.

686 Koster, R. D., and Coauthors, 2004: Regions of strong coupling between soil moisture and precip-  
687 itation. *Science*, **305 (5687)**, 1138–1140.

688 Levine, X. J., and W. R. Boos, 2017: Land surface albedo bias in climate models and its association  
689 with tropical rainfall. *Geophysical Research Letters*, **44 (12)**, 6363–6372.

690 Lindzen, R. S., and S. Nigam, 1987: On the role of sea surface temperature gradients in forcing  
691 low-level winds and convergence in the tropics. *Journal of the Atmospheric Sciences*, **44 (17)**,  
692 2418–2436.

693 Manabe, S., 1969: Climate and the ocean circulation: I. the atmospheric circulation and the hy-  
694 drology of the earth’s surface. *Monthly Weather Review*, **97 (11)**, 739–774.

695 Maroon, E. A., and D. M. Frierson, 2016: The impact of a continent’s longitudinal extent on  
696 tropical precipitation. *Geophysical Research Letters*, **43 (22)**, 11–921.

697 Neelin, D., and I. Held, 1987: Modeling tropical convergence based on the moist static energy  
698 budget. *Mon. Wea. Rev.*, **115**, 3–12.

699 Neelin, J. D., 2007: Moist dynamics of tropical convection zones in monsoons, teleconnections,  
700 and global warming. Princeton University Press, 267–301 pp.

701 Nie, J., W. R. Boos, and Z. Kuang, 2010: Observational evaluation of a convective quasi-  
702 equilibrium view of monsoons. *Journal of Climate*, **23** (16), 4416–4428.

703 Nieto Ferreira, R., and W. C. Chao, 2013: Aqua-planet simulations of the formation of the south  
704 atlantic convergence zone. *International journal of climatology*, **33** (3), 615–628.

705 Plumb, R. A., and A. Y. Hou, 1992: The response of a zonally symmetric atmosphere to sub-  
706 tropical thermal forcing: Threshold behavior. *Journal of the atmospheric sciences*, **49** (19),  
707 1790–1799.

708 Privé, N. C., and R. A. Plumb, 2007a: Monsoon dynamics with interactive forcing. part i: Ax-  
709 isymmetric studies. *Journal of the atmospheric sciences*, **64** (5), 1417–1430.

710 Privé, N. C., and R. A. Plumb, 2007b: Monsoon dynamics with interactive forcing. part ii: Impact  
711 of eddies and asymmetric geometries. *Journal of the atmospheric sciences*, **64** (5), 1431–1442.

712 Schneider, T., T. Bischoff, and G. Huag, 2014: Migrations and dynamics of the intertropical con-  
713 vergence zone. *Nature Review*, **513**, 45–53.

714 Schwingshackl, C., M. Hirschi, and S. I. Seneviratne, 2018: A theoretical approach to assess soil  
715 moisture-climate coupling across cmip5 and glace-cmip5 experiments. *Earth System Dynamics*,  
716 **9** (4), 1217–1234.

717 Seneviratne, S. I., T. Corti, E. L. Davin, M. Hirschi, E. B. Jaeger, I. Lehner, B. Orlowsky, and A. J.  
718 Teuling, 2010: Investigating soil moisture–climate interactions in a changing climate: A review.  
719 *Earth-Science Reviews*, **99** (3-4), 125–161.

720 Sharma, O., H. Le Treut, G. Seze, L. Fairhead, and R. Sadourny, 1998: Interannual variations  
 721 of summer monsoons: Sensitivity to cloud radiative forcing. *Journal of climate*, **11** (8), 1883–  
 722 1905.

723 Skinner, C. B., and N. S. Diffenbaugh, 2014: Projected changes in african easterly wave intensity  
 724 and track in response to greenhouse forcing. *Proceedings of the National Academy of Sciences*,  
 725 **111** (19), 6882–6887.

726 Smyth, J., S. Hill, and Y. Ming, 2018: Simulated responses of the west african monsoon and zonal-  
 727 mean tropical precipitation to early holocene orbital forcing. *Geophysical Research Letters*, **45**,  
 728 12,049– 12,057, doi:10.1029/2018GL080494.

729 Smyth, J. E., and Y. Ming, 2020: Characterizing drying in the south american monsoon onset  
 730 season with the moist static energy budget. *Journal of Climate*, 1–41.

731 Tomas, R. A., and P. J. Webster, 1997: The role of inertial instability in determining the loca-  
 732 tion and strength of near-equatorial convection. *Quarterly Journal of the Royal Meteorological*  
 733 *Society*, **123** (542), 1445–1482.

734 Vallis, G. K., and Coauthors, 2018: Isca, v1. 0: A framework for the global modelling of the  
 735 atmospheres of earth and other planets at varying levels of complexity.

736 Van Der Wiel, K., A. J. Matthews, D. P. Stevens, and M. M. Joshi, 2015: A dynamical framework  
 737 for the origin of the diagonal south pacific and south atlantic convergence zones. *Quarterly*  
 738 *Journal of the Royal Meteorological Society*, **141** (691), 1997–2010.

739 Walker, J. M., and S. Bordoni, 2016: Onset and withdrawal of the large-scale south asian monsoon:  
 740 A dynamical definition using change point detection. *Geophysical Research Letters*, **43** (22),  
 741 11–815.

- 742 Walker, J. M., S. Bordoni, and T. Schneider, 2015: Interannual variability in the large-scale dy-  
743 namics of the south asian summer monsoon. *Journal of Climate*, **28** (9), 3731–3750.
- 744 Wang, H., and R. Fu, 2004: Influence of cross-andes flow on the south american low-level jet.  
745 *Journal of climate*, **17** (6), 1247–1262.
- 746 Zhai, J., and W. Boos, 2015: Regime transitions of cross-equatorial hadley circulations with zon-  
747 ally asymmetric thermal forcings. *Journal of the Atmospheric Sciences*, **72** (10), 3800–3818.
- 748 Zhang, Y., and S. Fueglistaler, 2020: How tropical convection couples high moist static energy  
749 over land and ocean. *Geophysical Research Letters*, **47** (2), e2019GL086387.
- 750 Zhou, W., and S.-P. Xie, 2018: A hierarchy of idealized monsoons in an intermediate gcm. *Journal*  
751 *of Climate*, **31** (22), 9021–9036.

752 **LIST OF TABLES**

753 **Table 1.** JFM column-integrated MSE budget terms ( $\text{W m}^{-2}$ ) averaged over the South  
 754 American monsoon sector in the D0.26, R0.26, and W0.26 experiments. . . . . 37

755 TABLE 1. JFM column-integrated MSE budget terms ( $\text{W m}^{-2}$ ) averaged over the South American monsoon  
756 sector in the D0.26, R0.26, and W0.26 experiments.

	D0.26	R0.26	W0.26
$\bar{F}_{net}$	7.8	50.3	64.3
$\frac{\partial}{\partial t}\{\bar{\mathcal{E}}\}$	3.5	3.6	3.1
$\{\bar{\mathbf{v}} \cdot \nabla_p \bar{h}\}$	5.8	9.9	6.2
$\left\{\bar{\omega} \frac{\partial \bar{h}}{\partial p}\right\}$	-23.6	21.7	43.4
$\nabla \cdot \{\bar{h}' \bar{\mathbf{v}}'\}$	20.6	13.7	12.1

## LIST OF FIGURES

757			
758	<b>Fig. 1.</b>	Seasonal cycles of region-mean (a) precipitation, (b) surface temperature and insolation, and	
759		(c) net precipitation ( $P - E$ ) over the South American monsoon sector in the D0.26, R0.26,	
760		and W0.26 experiments. . . . .	39
761	<b>Fig. 2.</b>	JFM mean distributions of precipitation (shading) in $\text{mm d}^{-1}$ and 973 hPa MSE (contours)	
762		in Kelvin in the (a) D0.26, (b) R0.26, and (c) W0.26 simulations and (d) GPCP v2.3 1997-	
763		2015 precipitation observations. . . . .	40
764	<b>Fig. 3.</b>	JFM mean distributions of 920 hPa specific humidity (shading) and horizontal winds (vec-	
765		tors) in (a) D0.26, (b) R0.26, and (c) W0.26. . . . .	41
766	<b>Fig. 4.</b>	JFM mean vertical profiles of (a) vertical pressure velocity, (b) MSE, (c) DSE, (d) specific	
767		humidity, and (e) relative humidity in the three baseline experiments. . . . .	42
768	<b>Fig. 5.</b>	JFM distributions of the near-surface (973 hPa) MSE minus the tropical mean ( $30^\circ \text{ S}$ to	
769		$\text{N}$ ) value (shading) and precipitation in $\text{mm d}^{-1}$ (contours) in each of the three baseline	
770		experiments. . . . .	43
771	<b>Fig. 6.</b>	JFM mean precipitation in the monsoon sector as a function of land surface albedo with dry,	
772		wet, and realistic surface moisture conditions. . . . .	44
773	<b>Fig. 7.</b>	JFM mean vertical profiles of the vertical pressure velocity over the monsoon sector as	
774		land surface albedo is varied in the (a) dry, (b) realistic, and (c) wet land surface moisture	
775		experimental suites. . . . .	45
776	<b>Fig. 8.</b>	February 920 hPa absolute vorticity (contours) and divergence (shading) in the (a) D0.1, (b)	
777		D0.3, (c) D0.4, and (d) D0.5 simulations. The bold black line is the zero-line of absolute	
778		vorticity. . . . .	46
779	<b>Fig. 9.</b>	JFM mean precipitation in the monsoon sector as a function of (a) net column energy and	
780		(b) 973 hPa $\theta_e$ in all land surface albedo and moisture perturbation experiments. Panel (a)	
781		also includes the data for all four seasons of the GFDL AM4 control and +2-K SST warming	
782		experiments (labeled on the plot), as well as the four seasons of the D0.26 experiment (JFM,	
783		AMJ, JAS, OND). Panel (b) includes the seasonal data for the three baseline experiments. . . . .	47
784	<b>Fig. 10.</b>	A schematic overview of the monsoon circulation properties and relevant physical mecha-	
785		nisms across the land surface parameter space. . . . .	48

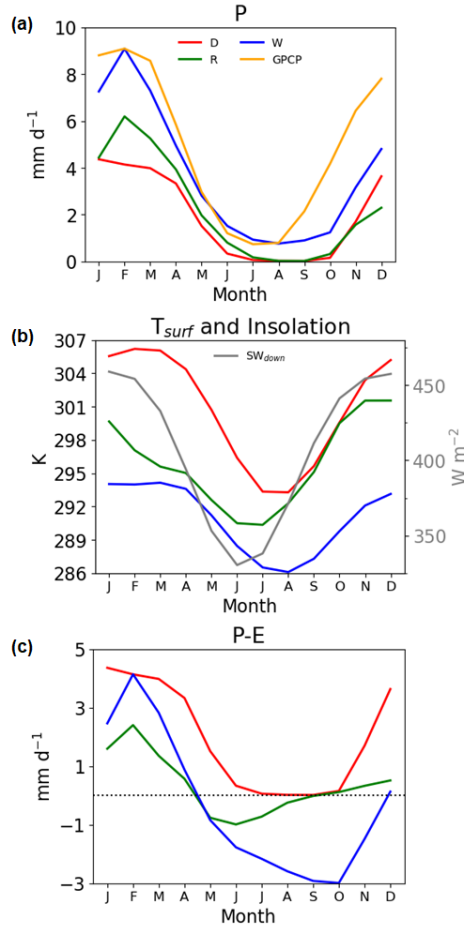
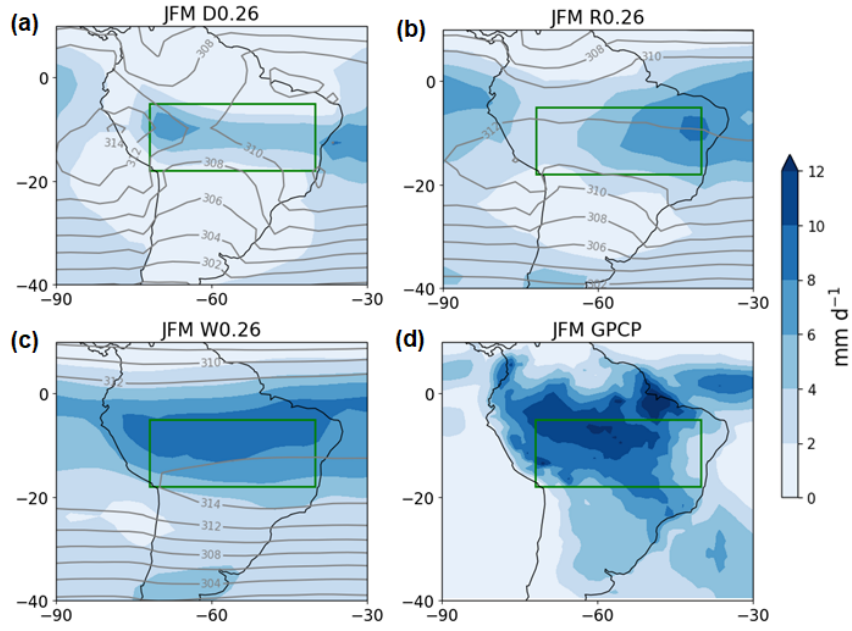


FIG. 1. Seasonal cycles of region-mean (a) precipitation, (b) surface temperature and insolation, and (c) net precipitation ( $P - E$ ) over the South American monsoon sector in the D0.26, R0.26, and W0.26 experiments.



788 FIG. 2. JFM mean distributions of precipitation (shading) in  $\text{mm d}^{-1}$  and 973 hPa MSE (contours) in Kelvin  
 789 in the (a) D0.26, (b) R0.26, and (c) W0.26 simulations and (d) GPCP v2.3 1997-2015 precipitation observations.

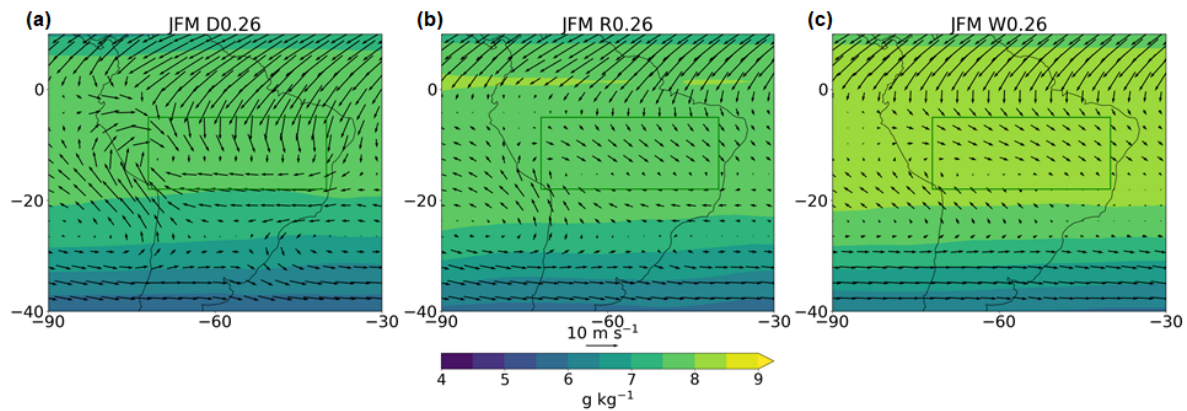


FIG. 3. JFM mean distributions of 920 hPa specific humidity (shading) and horizontal winds (vectors) in (a) D0.26, (b) R0.26, and (c) W0.26.

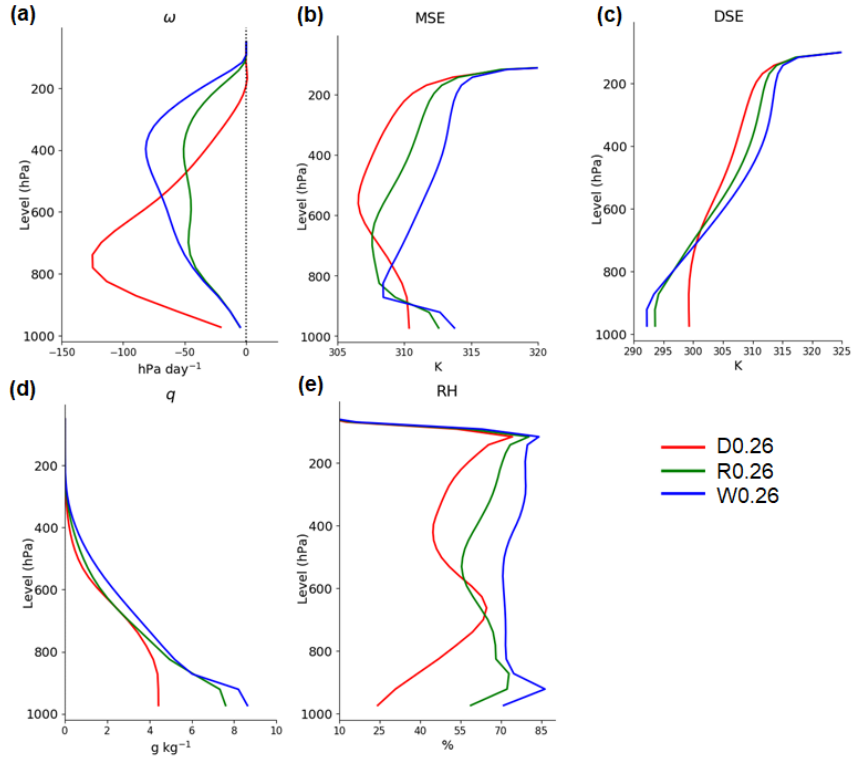
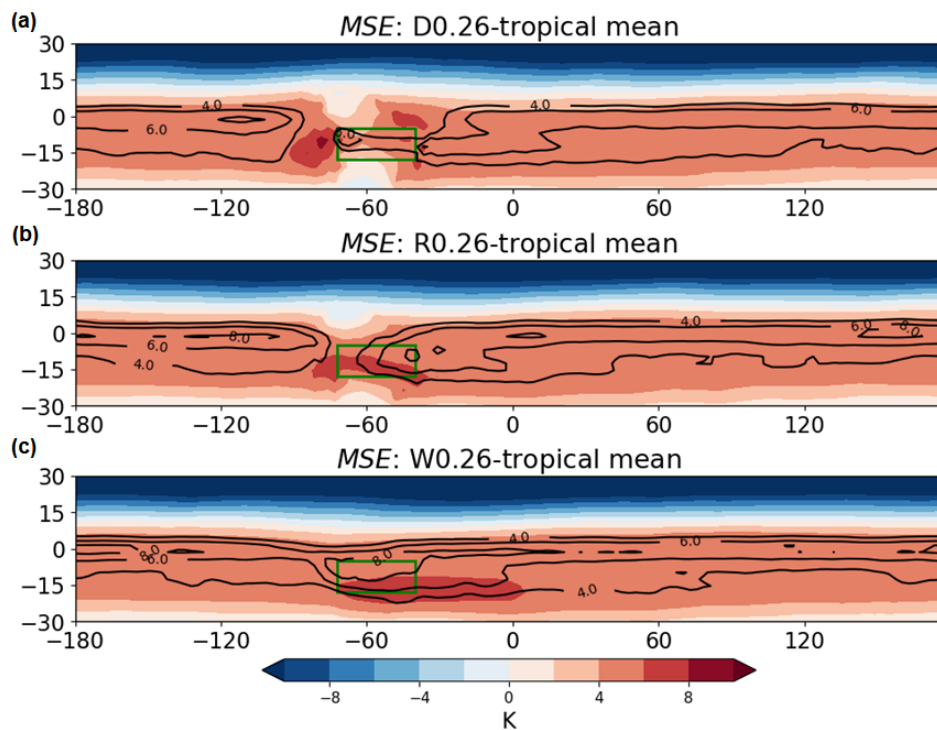
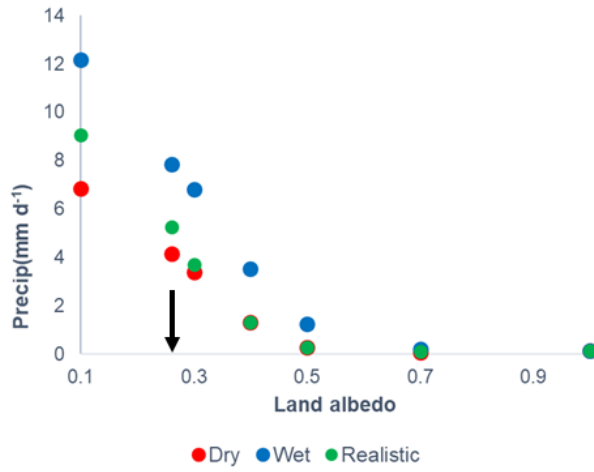


FIG. 4. JFM mean vertical profiles of (a) vertical pressure velocity, (b) MSE, (c) DSE, (d) specific humidity, and (e) relative humidity in the three baseline experiments.



794 FIG. 5. JFM distributions of the near-surface (973 hPa) MSE minus the tropical mean (30° S to N) value  
 795 (shading) and precipitation in mm d<sup>-1</sup> (contours) in each of the three baseline experiments.



796 FIG. 6. JFM mean precipitation in the monsoon sector as a function of land surface albedo with dry, wet, and  
 797 realistic surface moisture conditions.

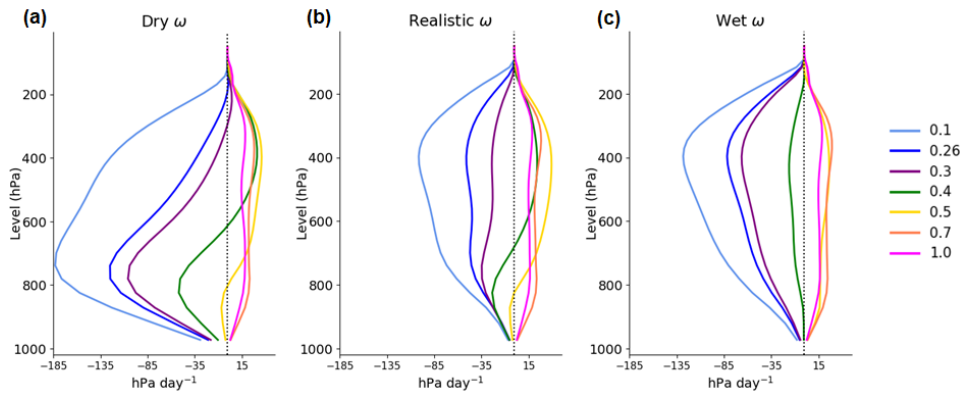


FIG. 7. JFM mean vertical profiles of the vertical pressure velocity over the monsoon sector as land surface albedo is varied in the (a) dry, (b) realistic, and (c) wet land surface moisture experimental suites.

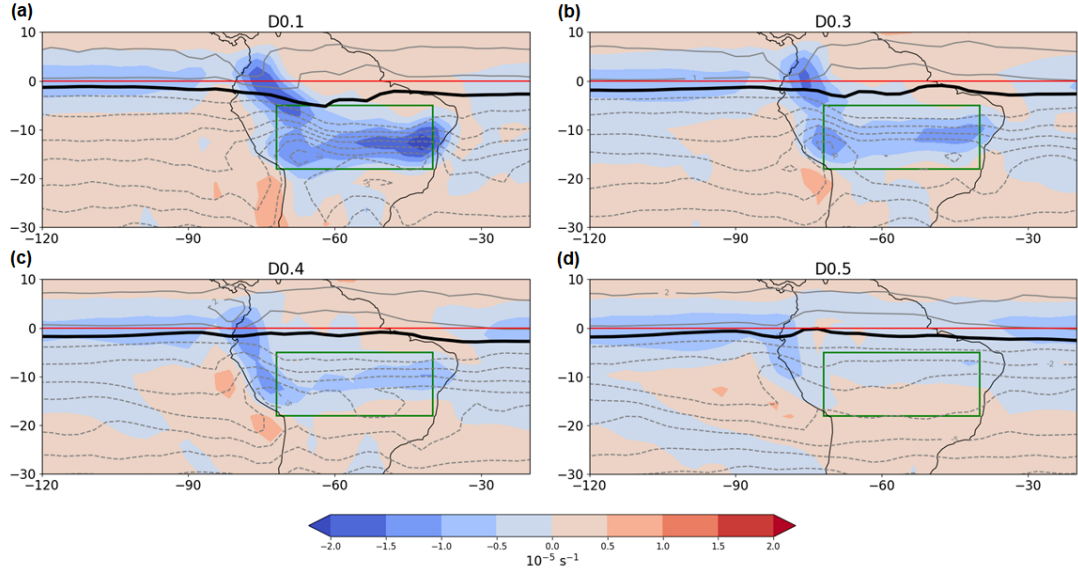


FIG. 8. February 920 hPa absolute vorticity (contours) and divergence (shading) in the (a) D0.1, (b) D0.3, (c) D0.4, and (d) D0.5 simulations. The bold black line is the zero-line of absolute vorticity.

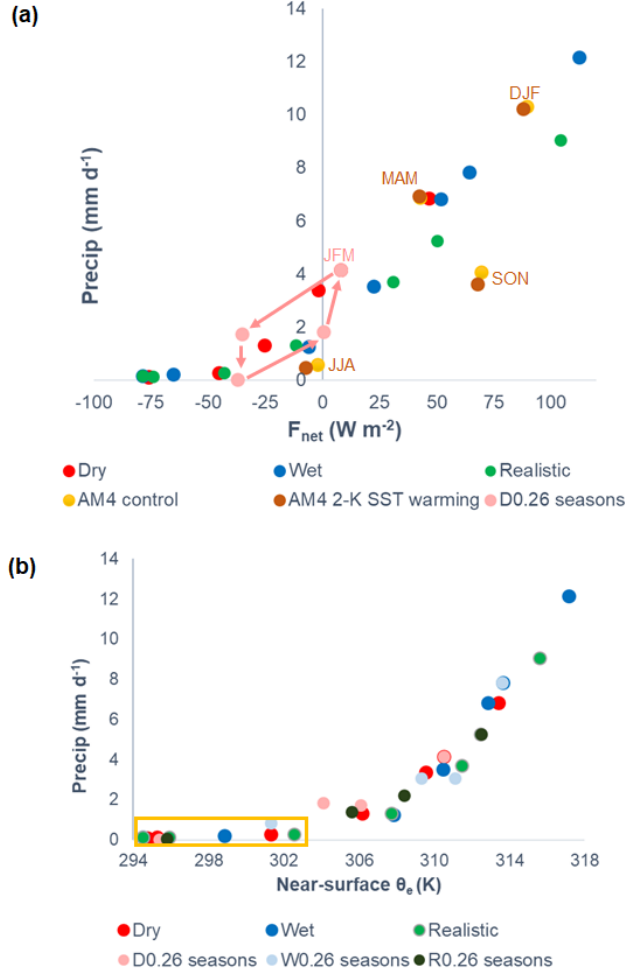


FIG. 9. JFM mean precipitation in the monsoon sector as a function of (a) net column energy and (b) 973 hPa  $\theta_e$  in all land surface albedo and moisture perturbation experiments. Panel (a) also includes the data for all four seasons of the GFDL AM4 control and +2-K SST warming experiments (labeled on the plot), as well as the four seasons of the D0.26 experiment (JFM, AMJ, JAS, OND). Panel (b) includes the seasonal data for the three baseline experiments.

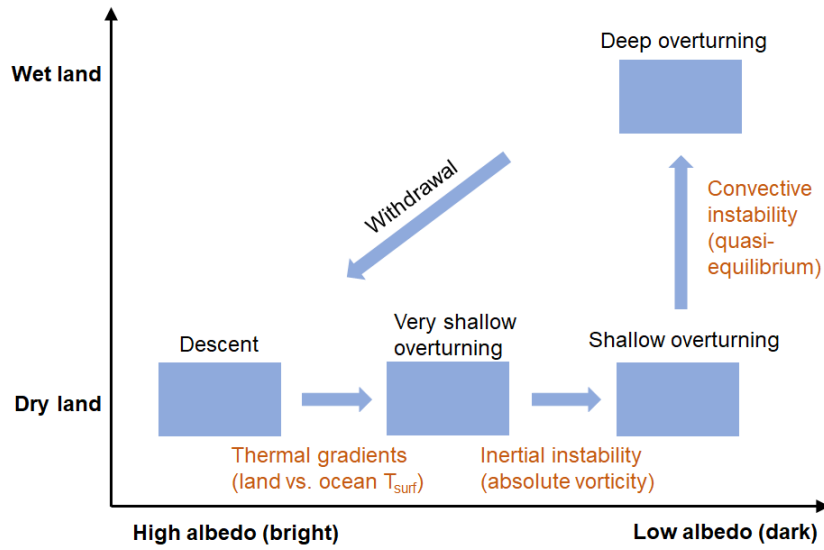


FIG. 10. A schematic overview of the monsoon circulation properties and relevant physical mechanisms across the land surface parameter space.